ADVANCED ENERGY MATERIALS
www.advenergymat.de

Lithium Dendrite Deflection at Mixed Ionic–Electronic Conducting Interlayers in Solid Electrolytes

Zikang Yu, Chenjie Gan, Aleksandar S. Mijailovic, Aidan Stone, Robert Hurt, Cristina Lopez Pernia, Xingcheng Xiao, Changmin Shi, and Brian W. Sheldon**

Solid state lithium metal batteries using garnet solid electrolytes such as LLZTO ($Li_{6.4}La_3Zr_{1.5}Ta_{0.5}O_{12}$) promise substantial improvements in energy density and safety. However, practical implementation is hindered by lithium dendrite penetration at high current densities. Recent work shows that internal electrochemically induced mechanical stresses are large enough to propagate lithium dendrites and subsequently fracture solid electrolytes. This study builds on this understanding and demonstrates that stress-driven dendrite propagation can be controlled via deflection at weakly bonded internal interfaces. This approach, based on a fracture-mechanics analysis of multilayered composites, is investigated with a variety of interlayer materials that are embedded into LLZTO. The viability and effectiveness of dendrite deflection are most clearly evident with reduced graphene oxide where the critical current density increased from 0.6 to 3.8 mA cm^{-2}. In this material, both the weak interface with LLZTO and the mixed ionic–electronic conducting nature of the interlayer appear to contribute to the improved performance. Additional insight into the mechanics of multilayered electrolytes is also obtained with finite element modeling. The overall results present a promising proof-of-concept demonstration along with important generalized design guidelines for creating multilayered solid electrolyte architectures that can enable high-performance solid-state batteries.

1. Introduction

All-solid-state lithium metal batteries have the potential to advance the mass commercialization of electric vehicles.[1] The solid electrolyte (SE) is at the core of these systems, and garnet solid state electrolytes such as $Li_{6.4}La_3Zr_{1.5}Ta_{0.5}O_{12}$ (LLZTO) have been widely investigated due to their relatively high ionic conductivity (≈0.1–1 mS cm^{-1} at 25 °C) and a wide electrochemical stability window.[2–5] One major limitation of LLZTO, however, is the formation of lithium filaments or "dendrites" that grow through the electrolyte and cause short-circuiting, uncontrolled discharge, and thermal runaway.[2–6] A multitude of recent studies have proposed that dendrite propagation in LLZTO occurs via a fracture-like mechanism, with the dendrite behaving like an internally loaded Griffith crack.[7–14] In this process, as the lithium-filled crack extends forward, the internal hydrostatic pressure is alleviated, but the continual flux of lithium into the dendrite repressures the filament and leads to additional crack extension. This continuous process results in dendrite propagation through the LLZTO, driven by internal pressure in the lithium filament. Several recent publications have proposed dendrite propagation mitigation strategies that are based on their stress-driven nature.[15,16] For example, Fincher et al. have directly shown that applied stresses can deflect dendrites in LLZTO.[13]

The general strategy of lithium dendrite deflection at an interlayer interface is inspired by laminated ceramic structures, where crack deflection can substantially increase the overall fracture resistance of the material.[17–19] Specifically, this behavior is enabled when a crack running through a composite ceramic material, upon reaching a bi-material interface, deflects and runs parallel along the interfacial layer for a substantial period instead of directly fracturing through the composite. This phenomenon can dramatically increase damage tolerance and delay the complete through-thickness fracture of the material. This suggests that it should be possible to similarly deflect pressure-driven lithium dendrites at bi-material interfaces in composite solid electrolytes.

In this work, we demonstrate that a fracture-mechanics framework accurately describes lithium dendrite deflection at an interlayer. The idea of dendrite deflection due to an elastic mismatch was proposed in a previous modeling study, without considering the role of interfacial debonding energies.[20] Experimental evidence of dendrite redirection at interfaces has been presented in several studies that use sulfide electrolytes.[21,22] However, the contact with Li causes these SE materials to decompose, which

Z. Yu, C. Gan, A. S. Mijailovic, A. Stone, R. Hurt, C. L. Pernia, C. Shi, B. W. Sheldon
School of Engineering
Brown University
Providence, RI 02912, USA
E-mail: changmin_shi@brown.edu; brian_sheldon@brown.edu
X. Xiao
General Motors Global Research and Development
General Motors Global Technical Center
Warren, MI 48092, USA

The ORCID identification number(s) for the author(s) of this article can be found under https://doi.org/10.1002/aenm.202403179

DOI: 10.1002/aenm.202403179

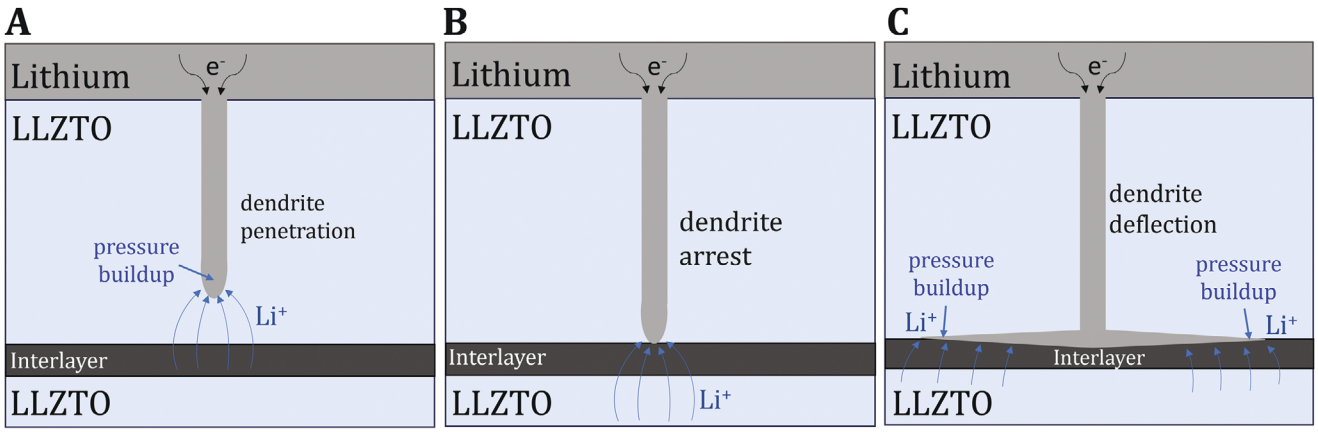

Figure 1. Models of dendrite penetration and deflection at interlayers within the solid electrolyte. A) Lithium dendrite penetrating through a solid electrolyte (LLZTO) before reaching the engineered interlayer. Lithium flux is concentrated at the dendrite tip. B) Shows a theoretically valid but unlikely complete dendrite arrest mechanism at the composite material interface between the LLZTO and the engineered interlayer. C) Shows Li dendrite penetration and deflection at an engineered interlayer.

makes it difficult to interpret the impact that stresses have on dendrite propagation and deflection at an internal interface. The stability of LLZTO with Li makes it a logical choice for investigating dendrite deflection. This was investigated by testing a variety of interlayers with vastly different properties. While a number of prior studies have examined LLZTO in multilayer structures, these generally employ coating layers between the lithium anode and solid electrolyte or use stacked heterogeneous electrolytes which do not provide direct information about dendrite deflection.[23–28] Of the materials that we investigated, the most effective was reduced graphene oxide (rGO), where mechanical and electrochemical effects appear to provide important synergistic benefits. By increasing the tortuosity of the dendritic path, dendritic deflection at these interlayers increases the work of fracture and substantially delays catastrophic lithium dendrite penetration and cell failure. Both analytical modeling and a finite element model (FEM) were used to elucidate the fracture-mechanics conditions for lithium dendrite deflection at these interlayers.

2. Results and Analysis

2.1. Mechanics of Dendrite Propagation and Deflection

Recent experiments and modeling efforts have proposed mechanics-based descriptions of lithium dendrite propagation.[7,8,12,13] Solid electrolyte fracture (and subsequent cell failure) is thermodynamically favorable when the elastic strain energy released due to lithium dendrite extension (G) reaches the fracture resistance of the material. Dendrite propagation through the solid electrolyte is shown in **Figure 1**A. There are several ways that introducing a bi-material interface can mitigate this process. Specifically, two different scenarios are assessed: 1) complete crack arrest and 2) crack deflection along the interface. The application of these ideas to a solid electrolyte with a general interlayer material is shown in Figure 1B,C.

Continuous Lithium flux into a lithium-filled dendrite will produce internal pressure that results in mechanical stress normal to the dendrite/solid electrolyte interface, $\sigma_{xx}^{flaw}(y)$. For a plane strain configuration (i.e., an infinitely thick SE slab), the Mode I stress intensity factor (SIF) for this internal loading is given by:[17,29,30]

$$K_I^f = \psi \sqrt{\pi\, c}\, \bar{p}_{eff} \tag{1}$$

where c is the flaw/crack length and:

$$\bar{p}_{eff} = \frac{2}{\pi} \int_0^c \frac{\sigma_{xx}^{flaw}(y)}{\sqrt{c^2 - y^2}}\, dy \tag{2}$$

The right side of this expression accounts for variations in the internal pressure along the length of the dendrite (which may occur due to dynamic effects). The factor ψ depends on the crack geometry: the planar edge crack in our case gives a $\psi \cong 1.12$. The corresponding strain energy release rate due to dendrite propagation is then given by:

$$G = \frac{K_I^2}{E'_{SE}} \tag{3}$$

where E'_{SE} is the plane strain modulus of the electrolyte. Fracture is expected when G exceeds the fracture resistance of the electrolyte (R_S). This condition is generally defined by the critical SIF, K_{Ic}:

$$K_I^f \geq K_{Ic} \tag{4}$$

where $R_S = K_{Ic}^2 / E'_{SE}$.

With a fixed value of $\bar{p}_{eff}$ and a strongly bonded interface, fracture stops if the second material has a fracture resistance, R_L, that is larger than that of the SE, and crack penetration into the second material occurs if $R_L \leq R_S$. If the crack arrest condition is met, it is often temporary, since the continuing lithium flux into a static lithium filament increases the pressure (i.e., a larger $\bar{p}_{eff}$ will increase K_I^f). However, fracture through this second material will be halted if the pressure completely counteracts the electrochemical driving force (i.e., $p = F\,\eta_P / V_m$, where p is the hydrostatic pressure in the dendrite, F is the Faraday constant, η_P is the

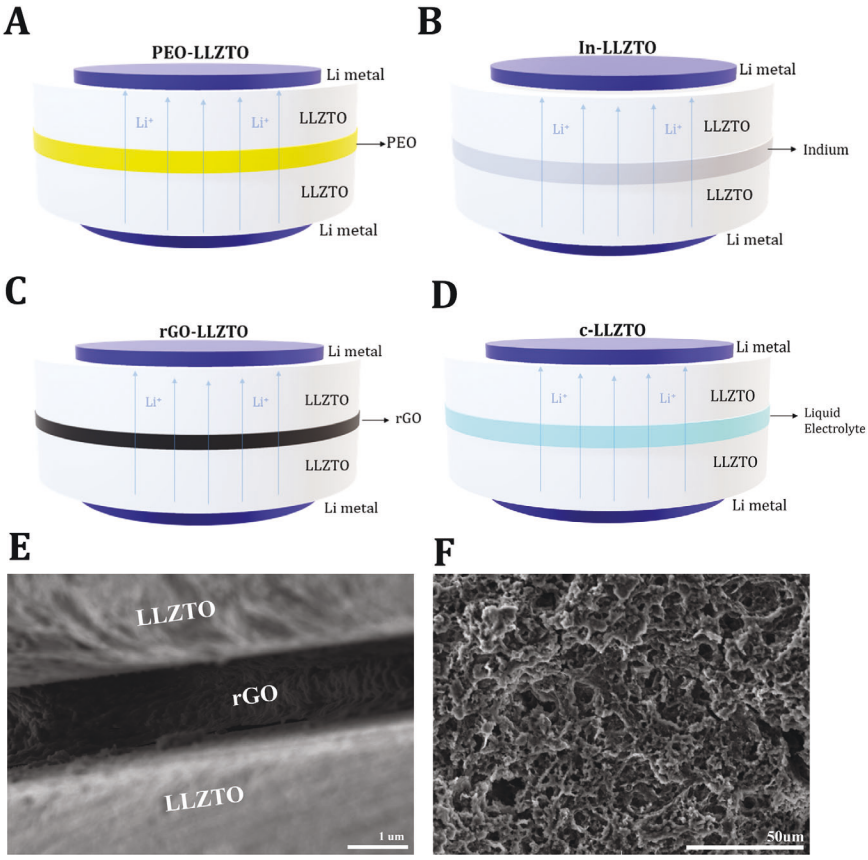

Figure 2. Schematics and Scanning Electron Microscope (SEM) images of engineered interlayer-electrolyte structures. A) PEO-LLZTO cell: Thin 1um PEO interlayer intercalated between two pieces of LLZTO. B) rGO-LLZTO cell: Thin 1 μm rGO interlayer intercalated between two pieces of LLZTO. C) In-LLZTO cell: Physical Vapor Deposition of ≈2.5 μm thin Indium metallic layer bonded between two pieces of LLZTO. D) c-LLZTO cell: Thin (<1 μm) liquid LiTFSI electrolyte layer intercalated between two pieces of LLZTO. E) SEM cross-section image of rGO-LLZTO. F) Plane view of rGO interlayer.

local overpotential, and V_m is the Li molar volume).[7,15] This thermodynamically defined limiting value is determined by the local overpotential (which can vary along the length of the dendrite). If this value exceeds the fracture threshold, then additional lithium flux into the dendrite should ultimately lead to continued propagation, rather than arrest (see Figure 1B). For this dendrite arrest case, the distinction here is between the measured overpotential (across the cell), and the local overpotential at the tip of the dendrite (where pressure in the dendrite can offset the local voltage drop). This effect means that the chemical potential difference at the tip is zero, even though there is a voltage drop here.

With a weakly bonded interface, crack deflection occurs instead (see Figure 1C). The energetics for this were analyzed by He and Hutchinson and others.[17,31] For materials with the same elastic modulus, the resulting criteria for deflection are:

$$\frac{\Gamma_D}{R_L} < \approx \frac{1}{4} \tag{5}$$

where Γ_D is the fracture resistance for the deflected (interface) crack. This interfacial property is a measure of the adhesion between the two materials (i.e., measured with the peel test described below), in contrast to R_L which is a bulk property (described above). We argue here that a similar energy-based analysis applies to the propagation of a pressurized lithium dendrite, and that deflection at weak interfaces is advantageous for designing interlayers that will mitigate dendrite penetration.

After the initial dendrite deflection occurs, its continuing propagation should differ from a deflected crack in several important ways. The pressure build-up inside of the deflected dendrite will create an elastic driving force that favors propagation along the interface. Thus, the stress field at the crack tip will initially include contributions from the pressure in both the interlaminar and the pre-deflection filaments (Figure 1C). The latter will dissipate as the tip moves further along the interface, and thus the stress field will approach pure Mode I loading (due to the internal pressure) after the deflected crack has run far enough. This differs from the conventional fracture case with external loading, where the deflected crack is subjected to a different combination of Mode I/Mode II contributions.

2.2. Laminated Electrolyte Architectures

Experiments were designed to investigate dendrite propagation and deflection at an engineered interlayer. To accomplish this, a variety of interlayers with drastically different material properties were constructed between two LLZTO discs. Four of these

Table 1. Descriptions of Major Cell Configurations tested in this work.

Cell name	Configuration description
PEO-LLZTO	1 μm thin PEO polymer interlayer laminated between two 500 μm thin LLZTO solid electrolytes
In-LLZTO	2.5 μm thin Indium interlayer laminated between two 500 μm LLZTO solid electrolytes using physical vapor deposition
rGO-LLZTO	1 μm thin rGO interlayer laminated between two 500 μm LLZTO solid electrolytes
c-LLZTO	Thin liquid Lithium bis(trifluoromethane) sulfonimide (LiTFSI) electrolyte film drop cast between two 500 μm LLZTO solid electrolytes
PVDF-HFP-LLZTO[a)]	1 μm thin Poly(vinylidene fluoride-co-hexafluoropropylene) (PVdF-HFP) polymer interlayer laminated between two 500 μm LLZTO solid electrolytes
rGO-PEO-LLZTO[a)]	2 μm thin composite interlayer (1 μm rGO interlayer + 1 μm PEO interlayer) laminated between two 500 μm thin LLZTO solid electrolytes

[a)] Data shown in Supporting Information.

configurations are depicted in **Figure 2**, and an expanded list is given in **Table 1**. These materials were selected to provide significant variations in three key properties: 1) the elastic modulus, 2) the interfacial fracture resistance, and 3) electronic conductivity (all materials are ionically conductive). Polyethylene Oxide (PEO) was first selected as a solid polymer electrolyte interlayer (labeled PEO-LLZTO in Figure 2A). Polymer electrolytes (such as PEO) have been explored more broadly to accommodate volume changes during electrochemical cycling.[32–37] Thus, PEO provides a simple basis for considering deflection based on elastic energies.

Indium, as a metallic interlayer, was used to test the effects of a both highly ionically and electronically conductive interlayer. Indium also alloys readily react upon contact with Li. The Indium-interlayer electrolyte is shown schematically in Figure 2B (In-LLZTO).

Reduced graphene oxide (rGO) was explored as a dynamic interlayer material with high fracture toughness[38] and limited electronic conductivity. For example, rGO can also be easily modified using a "skin-wrinkles-skin structure" that can drastically increase its fracture toughness.[38] To create this engineered interlayer, graphene oxide was synthesized using a modified Hummer's method and harvested into an aqueous GO ink for coating. The GO ink was then pipetted onto one LLZTO disc before capping the sandwich structure with a second LLZTO disc, and then thermally reduced to rGO. The electrolyte with the rGO interlayer is shown in Figure 2C, labeled rGO-LLZTO. Figure 2E,F show SEM morphology images of the rGO film.

Finally, Figure 2D shows the design for a control experiment with no engineered interlayer, in which only a thin liquid electrolyte film was inserted between two LLZTO discs (c-LLZTO) for improved contact and cell cycling feasibility. In this configuration, stress generated by the dendrite in the upper layer will not be transferred to the lower layer. In this case, dendrite deflection due to mechanical effects is not expected to occur.

2.3. Electrochemical Results

Lithium dendrite penetration is typically assessed by measuring critical current density (CCD), which is determined by incrementing the current during symmetric plating-stripping cycles and defining the CCD as the value where the cell fails. However, as this work focuses on exploring the feasibility of dendrite deflection at different interlayers, a unidirectional plating-only electrochemical protocol is primarily used instead. This approach makes it possible to specify the LLZTO layer where lithium dendrite growth initiates (adjacent to the plating Li electrode) and directly observe the electrochemical signal once the lithium dendrite reaches the interlayer. Focusing dendrite propagation on one side of the multilayered electrolyte thus enables a targeted study of dendrite-interlayer interactions that excludes complications introduced during Li stripping. For this unidirectional plating-only procedure, the plating was initiated at a 0.1 mA cm^{-2} current density, with increments of 0.05 mA cm^{-2} and a 1 mAh cm^{-2} capacity limit per step. The lithium plating direction (i.e., Li^+ ion flux) is represented by light blue arrows in Figure 2A–D, with lithium dendrite propagation occurring downward in all scenarios.

The c-LLZTO control cells provide a basis for comparing solid electrolytes with different engineered interlayers. **Figure 3A** shows data for a typical control cell, without any engineered interlayer, in which cell failure occurs at 0.6 mA cm^{-2}. Here, lithium dendrite penetration occurs through both LLZTO discs relatively easily, without any evidence of partial short-circuiting and recovery. A pressurized dendrite in the first LLZTO layer will not lead to a stress field in the second LLZTO layer (i.e., there is no load transfer) when a liquid electrolyte interlayer is used. In contrast, if localized lithium dendrite deflection occurs at a solid interlayer, a different overpotential signature will manifest to reflect this. With this in mind, the results with the c-LLZTO cells are important because they demonstrate that dendrite deflection does not occur when there is no load transfer between the layers.

The PEO interlayer has weak interfacial adhesion and a low elastic modulus, both of which promote deflection, as indicated by Equation (5). The low adhesion energy between PEO and LLZTO was measured independently with a peel test. The results in the Supporting Information show that this adhesion energy is ≈6 J m^{-2}, which is much lower than the estimated PEO fracture resistance (R_L in Equation (5)).[39] Based on this comparison, pure mechanical loading should induce crack deflection at this PEO/LLZTO interface, and by analogy lithium dendrite deflection is also expected. Figure 3B shows the electrochemical response of the PEO-LLZTO cell from plating-only cycles. At ≈0.85 mA cm^{-2}, there is a small decrease in the overpotential, indicating that a localized lithium dendrite has likely penetrated through the top LLZTO layer and reached the PEO interlayer. This distinctive overpotential drop occurred in all PEO-LLZTO cells that were tested. The overpotential value then stabilizes, which is consistent with temporarily trapping the lithium

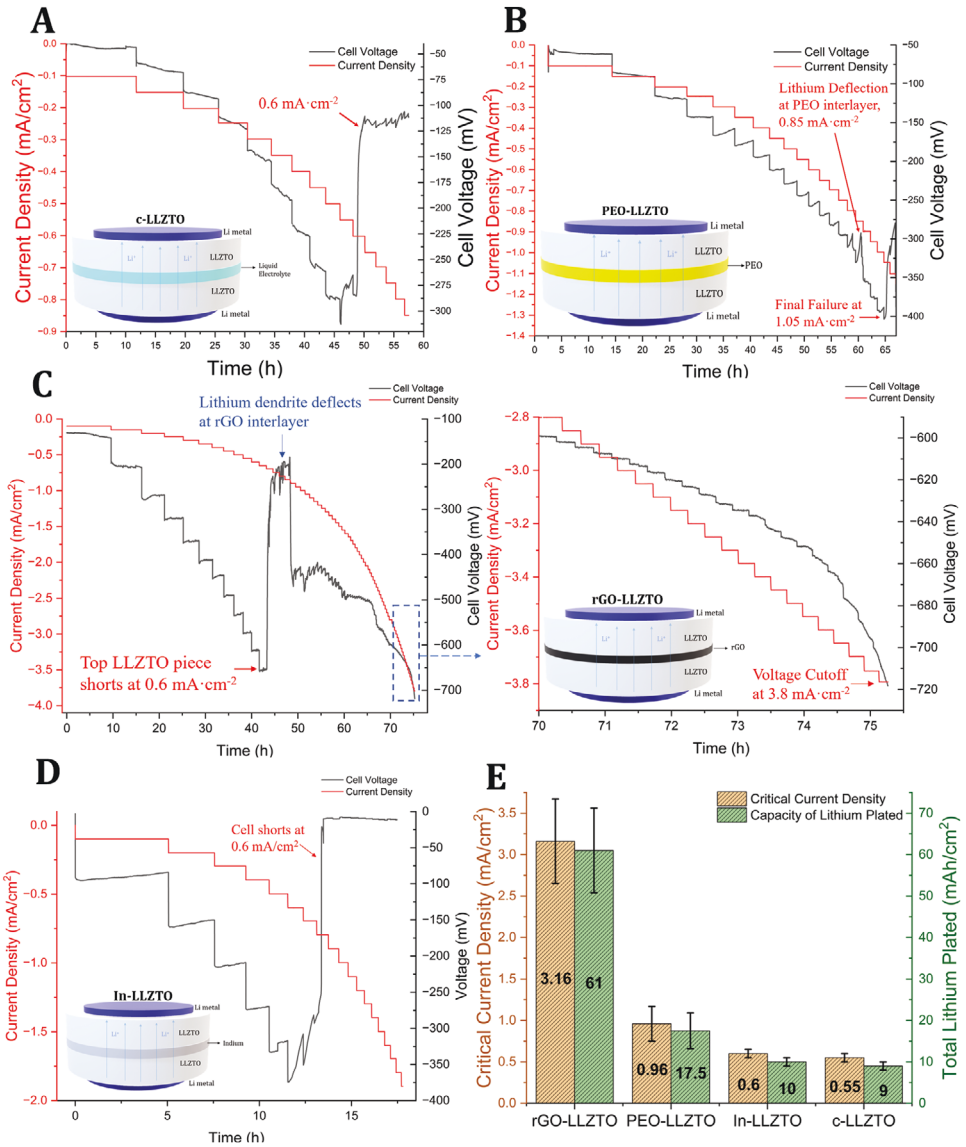

Figure 3. Electrochemical performance of different electrolytes. A) c-LLZTO electrochemical plating response. A total short-circuit occurs at 0.6 mA cm^{-2}, with no evidence of a partial shortcircuit and recovery. B) PEO-LLZTO electrochemical plating response. Cell experiences a small overpotential drop at 0.85 mA cm^{-2}, indicative of the small amount of lithium dendrite deflection on the PEO interlayer. The cell eventually short-circuits at 1.05 mA cm^{-2}. C) rGO-LLZTO electrochemical plating response (left); zoomed-in section of the final 70th–76th hours (right). The solid electrolyte with the rGO interlayer exhibits a much higher current density of 3.8 mA cm^{-2} at which point a potentiostat voltage cutoff stopped the test. The Electrochemical Impedance Spectroscopy (EIS) spectra collected (shown in the SI) indicate that the cell is short-circuited due to dendrite penetration. D) In-LLZTO electrochemical plating response. A total short-circuit occurs at 0.6 mA cm^{-2} with no evidence of partial short-circuit and recovery. E) Summary of the cell configurations tested in this work, with the average CCDs and average total capacity of lithium run for each engineered configuration. Capacity measurements are based on the lithium current density and plating time. The error bars correspond to the standard deviations for these measurements.

dendrite at the PEO interlayer interface without further penetration into the bottom LLZTO. The cell in Figure 3B then finally experiences a total short-circuit at 1.05 mA cm^{-2}, which corresponds to eventual catastrophic dendrite penetration through the second LLZTO layer. Data for the two other configurations using polymer electrolytes (PVDF-HFP-LLZTO and rGO-PEO-LLZTO), presented in the Supporting Information, provides additional evidence for the deflection phenomenon.

The rGO materials, similar to the polymer materials, are expected to exhibit weak bonding to oxide materials, with adhesion energies on the order of ≈10 J m^{-2}.[40,41] Figure 3C shows the electrochemical data for the rGO-LLZTO cell configuration. At a current density of 0.6 mA cm^{-2}, a dramatic overpotential decrease from ≈650 to ≈200 mV occurs. Similar to the PEO cells, this is consistent with localized lithium dendrite penetration through one LLZTO layer. After reaching the interlayer, the cell overpotential then remains relatively stable for subsequent cycling. This is consistent with lithium dendrite "deflection" along the rGO/LLZTO interface. This phenomenon resembles the PEO results, but the additional limited electronic conductivity of the rGO

material precipitates simultaneous qualified lithiation of the rGO interlayer (somewhat similar to the expected lithium alloying of the Indium metal interlayer). This implies that dendrite deflection here is affected by the synergistic mechanical and electrochemical phenomena. This phenomenon, present in all rGO-LLZTO cells, shows that the key advantage of the rGO-LLZTO design is that it can continue to cycle normally at high current densities despite dendritic penetration through one LLZTO layer.

In contrast, the In-LLZTO (fully metallic interlayer design) shows cell failure at 0.6 mA cm^{-2} with no evidence of a partial short-circuit or dendrite deflection (Figure 3D). Indium metal is known to have strong adhesion to oxide ceramic materials.[42,43] This property should preclude dendrite deflection due to weak interfacial bonding. In In-LLZTO, as the lithium dendrite penetrates through one LLZTO half and reaches the Indium interlayer, the high electronic conductivity of the Indium ($\approx 10^7$ S m^{-1}) should allow rapid lithiation of the entire interlayer (i.e., forming an In–Li alloy). There is no evidence of this in the electrochemical response, suggesting that direct lithiation of the metal interlayer does not alter the dendrite penetration path. This indicates that dendrite penetration into the lower layer occurs rapidly.

Figure 3E compares the CCD and total lithium capacity for the various interlayer-engineered electrolytes that were investigated. Additional details (including symmetric plating/stripping cycling tests) for all of these materials can be found in the Supporting Information. The overall results indicate that dendrite deflection occurs at all weakly bonded interfaces. Virtually all of these specimens (>20) exhibited the partial short-circuit associated with dendrite penetration of only the first LLZTO layer. The rGO interlayer enabled a particularly large increase in the CCD, and additional investigations were conducted with these materials to provide additional insight.

2.4. Expanded Study of rGO Interlayers

Three-electrode measurements were conducted to confirm that the rGO interlayer was lithiated after the initial overpotential drops that are attributed to the dendrite penetration of the first LLZTO layer. These cells were constructed with a copper tab extending into the cell and in contact with the rGO interlayer (**Figure 4A**). As a reference, an rGO lithiation reference cell was built to observe the voltage change of the rGO during direct lithiation (Figure 4B). The copper tab in the three-electrode cell allows measurement of the voltage change of the rGO interlayer versus Li during cycling to compare with the lithiation curve of the lithiation control cell rGO. In Figure 4B, the cell overpotential (black) experiences a rapid impedance drop that is indicative of lithiation of the rGO interlayer. This is nearly identical to the rapid drop in the voltage of the rGO interlayer versus lithium (red curve) in Figure 4A, thus confirming that the rGO interlayer is indeed lithiated after dendrite penetration of the first LLZTO layer. As the lithiation of the rGO interlayer is extremely localized and random, we cannot predict where in the interlayer the rGO becomes lithiated; thus, copper wires were placed at random in this interlayer in multiple experiments. In the successful case shown here, the copper wire was in the immediate vicinity of the localized rGO lithiation to detect this voltage change, while many of the other measurements did not show evidence of lithiation. These combined results are consistent with the lithiation of the rGO that is localized near the location where the dendrite penetrates through the first LLZTO layer.

The main advantage of the rGO-LLZTO design is its tolerance of high instantaneous current densities. However, longer symmetric lithium plating-stripping experiments were also used to evaluate the stability and longevity of the interlayer design. At a constant symmetric plating-stripping current of 0.5 mA cm^{-2} and 0.5 mAh cm^{-2} capacity/half cycle, the result for rGO-LLZTO in Figure 4C shows stable cycling for over 500 h without short-circuiting. The small overpotential drop from ≈0.49 to ≈0.4 V after 300 h most likely indicates localized lithium dendrite penetration through one LLZTO disc. This is consistent with the proposed mechanism, where the dendrite is trapped in the rGO interlayer, and the cell continues to cycle stably for an additional 200 h before short-circuiting. In contrast, the c-LLZTO control cell (Figure 4C, red curve) short-circuits after ≈170 h.

Post-mortem imaging of the samples is also consistent with successful dendrite deflection at the interlayer. The images in **Figure 5** show that lithium dendrite deflection at an engineered interlayer leads to dramatic differences in the dendrite penetration morphology. In all of these cases, lithium is plated on the top surface (i.e., the Li dendrite will grow from the top LLZTO disc and intersect the interlayer at the LLZTO (top)/interlayer interface). Figure 5A shows metallic lithium intercalated into the rGO after lithium dendrite deflection. To image the LLZTO after short-circuiting, the rGO and lithium were carefully removed. If lithium dendrite deflection occurs at the interlayer, the top and bottom LLZTO discs should show dendrite penetration sites at significantly different locations. The cross-sectional imaging in Figure 5B shows a thin lithium layer on top of the rGO interlayer. In Figure 5C, the dark region circled in red on the top LLZTO disk is indicative of a localized lithium dendrite penetration spot. This type of dark spot or line is often observed on LLZTO after short-circuiting and it is indicative of a lithium dendrite.[44,45] The lower LLZTO piece from the same experiment (Figure 5D) shows a drastically different pattern, with multiple penetration lines. This phenomenon is also observed for the PEO-LLZTO cell: In the top LLZTO piece (Figure 5E), the lithium dendrite penetrates at a localized area in the bottom right quadrant. The lower LLZTO piece from the same experiment (Figure 5F) also shows a multiple-penetration-line pattern. To confirm that these dark regions correspond to lithium dendrites, the LLZTO was carefully fractured directly along these dendritic "lines". Examination of the cross-section of these dendritic lines in the bottom LLZTO piece shows the characteristic "hexagonal honeycomb" or "web-like" morphology that has been widely reported for lithium dendrites in LLZTO, as seen in Figure 5G.[45] Our interpretation of the observations in Figure 5A–G is that the primary lithium dendrite penetrates through the top LLZTO at one location and that after deflection at the rGO or PEO interlayer, the lithium is dispersed laterally from this location. Penetration through the lower LLZTO piece then appears to occur via dendrite re-initiation at multiple sites in the lower LLZTO electrolyte.

This pattern of multiple penetration events is not observed in specimens where the electrochemical measurements do not show evidence of deflection, such as c-LLZTO and In-LLZTO. In c-LLZTO, the dendrite penetrates directly through the top and

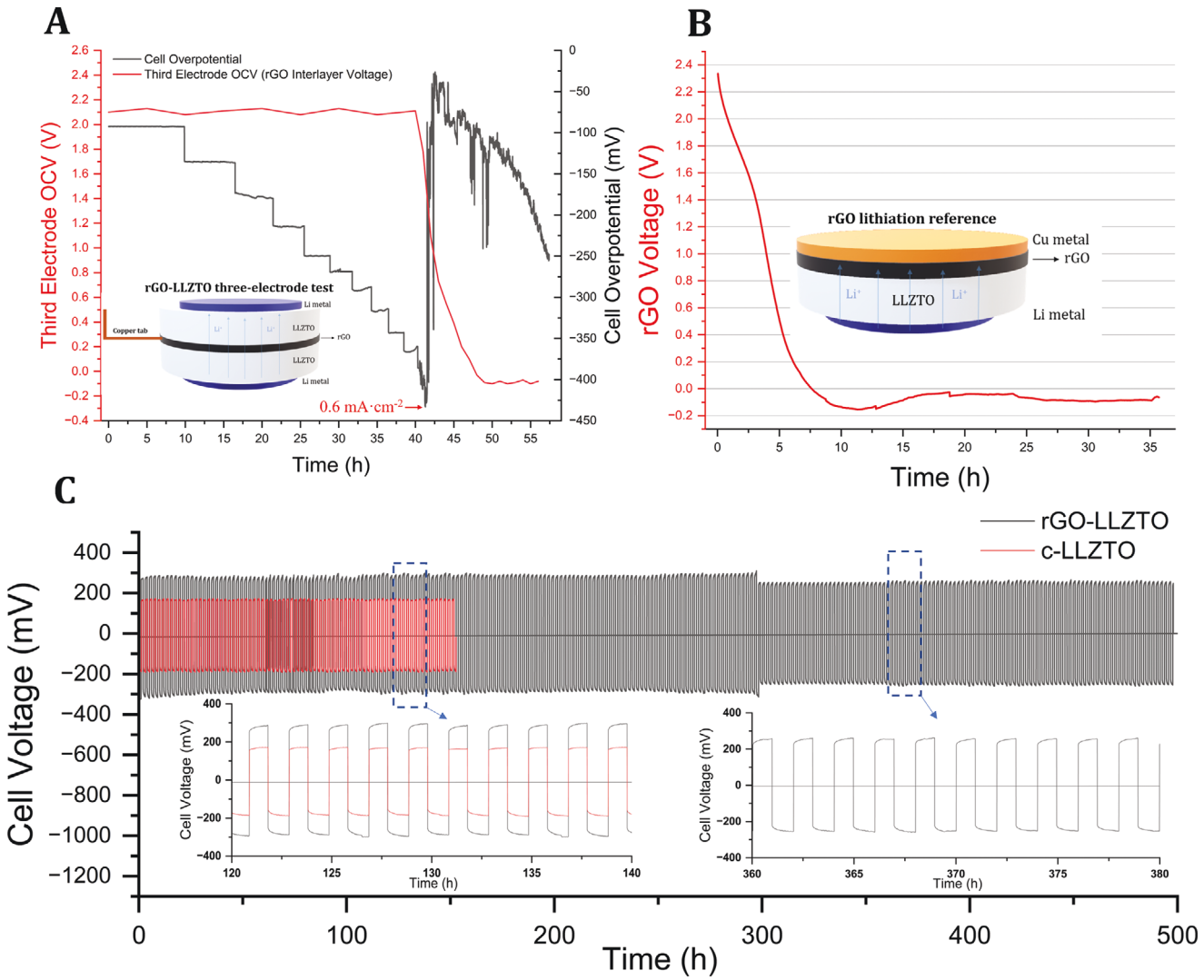

Figure 4. Expanded electrochemical study of rGO interlayer. A) Three-electrode cell Open Circuit Voltage (OCV) and cell overpotential overlapped; the rGO interlayer OCV (in red) corresponds to the measured potential difference between the rGO interlayer and Li counter electrode; Cell Overpotential (in black) corresponds to the voltage difference between the top working electrode and bottom counter electrode. Three-electrode-cell schematic is shown in the inset. B) 1 µm thin rGO layer lithiation voltage response under constant 0.1 mA cm^{-2} plating current. C) Long-term cycling comparison of rGO-LLZTO and c-LLZTO at 0.5 mA cm^{-2} symmetric current and 0.5 mAh cm^{-2} capacity limit.

bottom LLZTO pieces with minimal change in dendrite path, and the dendrite penetration locales are generally aligned between the top and bottom pieces, as shown in Figure 5H,I. On the other hand, in both rGO-LLZTO and PEO-LLZTO, the disparity in the patterns on the top and bottom – (single vs multiple events) demonstrates that the PEO and rGO interlayer completely alter the dendrite penetration path. This is clear evidence of increased "damage tolerance" to lithium dendrite penetration through the solid electrolyte, due to dendrite deflection laterally across the interlayer instead of directly penetrating through the full multilayer SE. This is analogous to the enhanced fracture resistance and damage tolerance that is commonly obtained with multilayered composites or coatings.[18,21,46] With rGO and PEO interlayers, lithium plating at this upper interface is consistent with a weak interface and the deflection criteria that are proposed in Section 2.1.

2.5. Mixed Ionic–Electronic Conducting Interlayer (rGO)

Of the materials that were investigated, the rGO interlayer is far better at mitigating dendrites. This is consistent with the mechanics analysis presented previously, in light of the fact that rGO has a high through-thickness fracture resistance and low interfacial adhesion with LLZTO. The PEO and rGO both have weak interfaces with LLZTO, and deflection is observed in both cases. However, rGO is a mixed ionic electronic conductor (MIEC), which suggests that this difference may be related to improved performance. While the In-LLZTO also employs an MIEC interlayer, deflection did not occur here, and the CCD was substantially lower. Although rGO and Indium are both mixed conductors, it appears that the Indium does not lead to dendrite deflection due to its high interfacial adhesion with LLZTO. The electronic conductivity of Indium metal is roughly six orders of

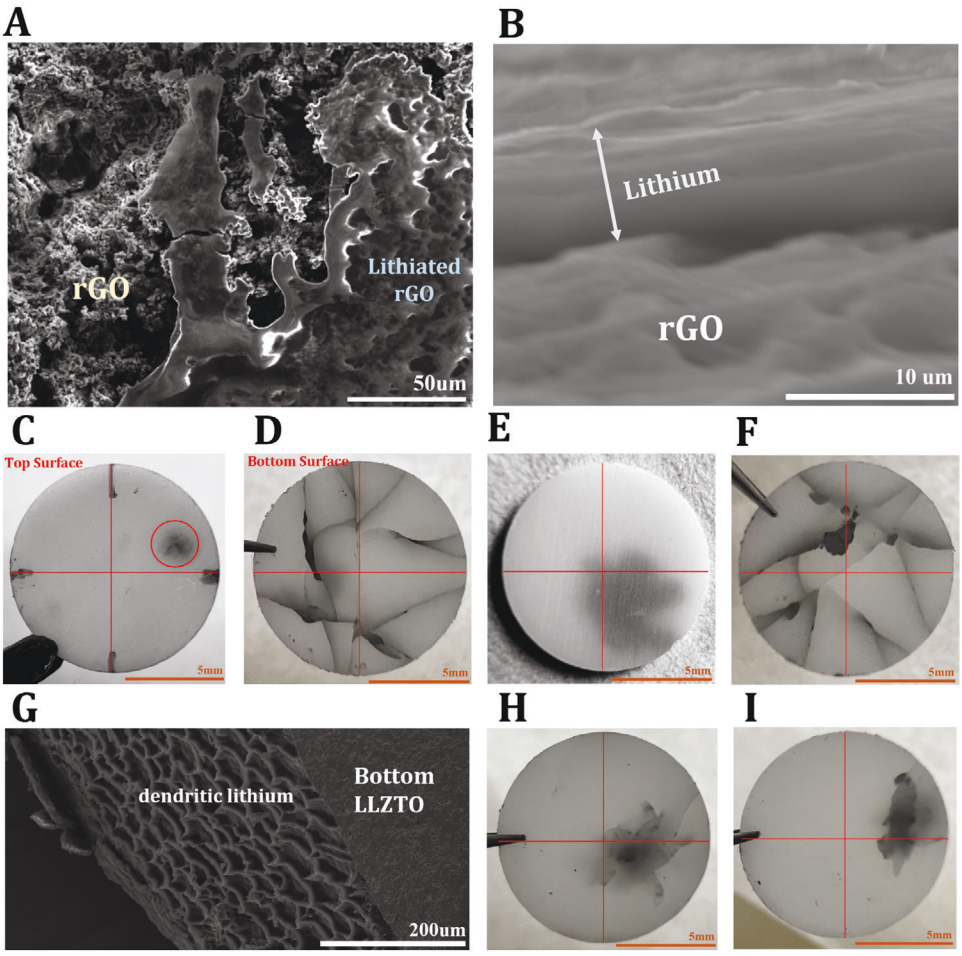

Figure 5. Visual evidence of dendrite deflection/penetration on interlayers after plating-only cycling. A) The two LLZTO discs were carefully pried apart to expose the rGO interlayer. Top–down SEM image shows shiny metallic lithium deflected on the rGO interlayer. B) SEM cross sectional imaging shows an 8μm layer of lithium scattered on top of the rGO interlayer after deflection. C) rGO-LLZTO: Lithium dendrite penetration at the top LLZTO piece after all the lithium and rGO has been polished off. A localized dendrite penetration spot is circled in red. To clarity the location comparison, both LLZTO discs are marked into four quadrants. D) rGO-LLZTO: Multiple lithium dendrite penetration lines spread laterally through the bottom LLZTO piece of rGO-LLZTO. E) PEO-LLZTO: Lithium dendrite penetration through the top LLZTO piece after a short circuit. The lithium dendrite penetration locale is in the rightmost quadrants. F) PEO-LLZTO: Multiple lithium dendrite penetration lines spread laterally through the bottom LLZTO piece of PEO-LLZTO. G) Cross-sectional image of "weblike" lithium dendrite after fracturing along a dendritic penetration line in Figure 5F. H) c-LLZTO: Lithium dendrite penetration through the top LLZTO piece after a short circuit. The lithium dendrite penetration locale is in the rightmost quadrants. I) c-LLZTO: Lithium dendrite penetration through the bottom LLZTO piece after a short circuit. The lithium dendrite penetration locale is also in the rightmost quadrants.

magnitude higher than that of rGO, and thus this property does not appear to be the dominant factor that dictates dendrite deflection. These comparisons indicate that a weakly bonded interface is critical to deflection, but that mixed conduction may also play an important role in the improved deflection performance obtained with the rGO-LLZTO. A schematic illustrating the behavior observed in this material is shown in **Figure** 6A. The lithium dendritic protrusions here are shown as flat ribbon-like structures that penetrate through the LLZTO and deflect at a weak interface with the rGO interlayer. While the mechanics-based analyses of dendrite deflection still apply to this mixed conducting interlayer, an additional coupled electrical effect is also in play because rGO conducts lithium and also has a non-negligible variable electrical conductivity of 0.9–58 S m^{-1} (based on four-point probe measurements). Thus, once a dendrite reaches the interlayer, electron conduction through the lithium can enable partial lithiation of the rGO.

The electrical conductivity of the interlayer complicates the interpretation of electrochemical measurements, as the measured overpotential will be affected by contributions from both lithiation of the MIEC interlayer (near the dendrite) and normal plating that occurs far away from the dendrite. Addressing this in detail requires additional experiments and modeling. One important concern here is the overall amount of lithium that enters the rGO after dendrite penetration through the first layer. If this interlayer is fully lithiated it will effectively act like a working electrode. For the experiment shown in Figure 3C, an estimated 6% of the interlayer capacity is lithiated (see Supporting Information for quantitative details). This implies that the electrical conductivity in these materials is low enough to limit full lithiation, and that

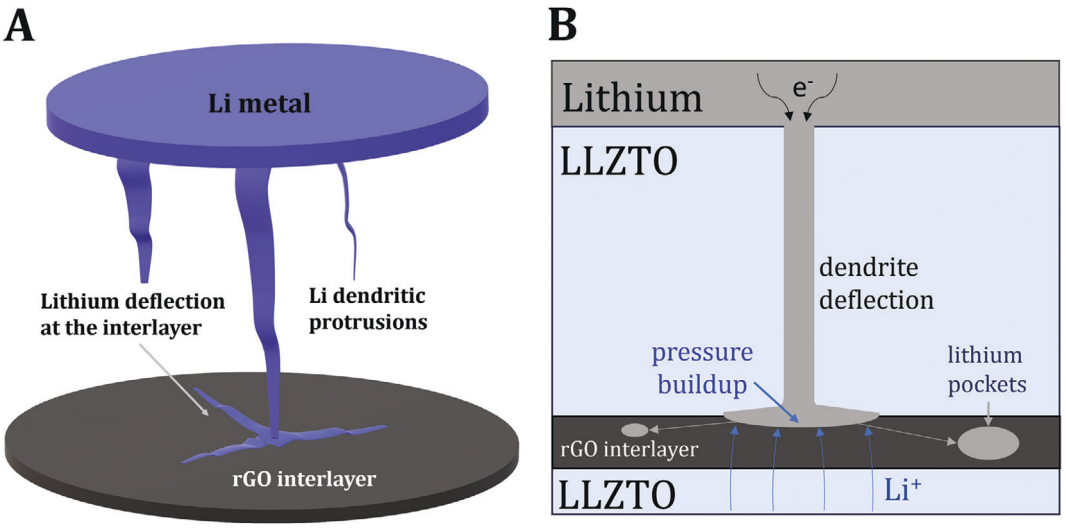

Figure 6. Lithium dendrite deflection at a mixed ionic–electronic conducting interlayer such as rGO. A) Schematic of dendritic deflection within the rGO interlayer. Metallic lithium is shown in blue, penetrating through a (transparent) LLZTO disc and deflecting in various directions upon reaching the rGO interlayer, shown in black. B) Mixed modes of both Li dendrite deflection and Li intercalation into a mixed ionic electronic conductor such as rGO.

lithiation of the rGO is localized near the location where the dendrite intersects the interlayer. The total amount of lithium lost to the rGO here is ≈0.07 mAh cm^{-2}, which is only 0.1% of the total lithium cycled in this experiment. This estimate shows that rGO lithiation does not substantially alter the overall cell capacity. This is further demonstrated with the long-term electrochemical tests reported in Figure 4C, where lithium stripping cycles were also employed. Based on these results, the small amount of lithium lost to the rGO suggests that this type of interlayer can deflect a dendrite without significantly limiting overall cell performance. It is anticipated that in thinner, sub-micron rGO interlayers the amount of lithiation would be reduced further, and thus have a negligible impact on overall capacity.

The schematic in Figure 6B illustrates several expected behaviors for the lithium dendrite after it reaches the rGO interlayer, starting with a lithiation front that begins at the tip and moves out into the interlayer. Localized lithiation might also occur away from this region, due to inhomogeneities in the interlayer material, shown schematically by the lithium "pockets." This particular material has a complex structure with PVDF-HFP binder and some nanoscale porosity, which is expected to lead to uneven lithiation, possible void formation during de-lithiation, and a complex stress distribution inside of the interlayer. An examination of these effects is beyond the scope of the current study, although control of these heterogeneities, along with control of the electrical conductivity, could potentially enable the design of interlayers with even better performance. The progressive lithiation of rGO should also induce pressure buildup inside the interlayer as lithiation proceeds. However, with this occurring inside of the lithiated rGO material, the impact of internal pressure on fracture along the rGO/LLZTO interface is likely to be more complex. It is possible (and perhaps likely) that the propagation of a lithiation front will instead be largely associated with direct lithiation of the active material that will generate pressure (i.e., compressive stress) inside of the lithiated material, and tensile stress in front of the lithiated region. It is also well established that the electric field in a solid electrolyte (an electric insulator) focuses the lithium-ion flux at the dendrite tip, thus rapidly increasing internal pressure buildup at this tip and accelerating dendrite growth (as illustrated in Figure 1A).[47,48] Within an electrically conducting interlayer such as rGO, however, the electric field will be redistributed due to the excess available electrons. The corresponding lithium flux will be less concentrated at the dendrite tip, (illustrated in Figure 6B) leading to decreased internal pressure at this tip, which could mitigate dendrite growth.

During traditional through-thickness fracture of layered composite structures, a mechanical crack that deflects along an interface will typically kink out of the interface, leading ultimately to complete through-thickness fracture.[17,31] Lithium dendrites should exhibit similar behavior, in ways that might ultimately lead to a short circuit. For both cases, "kinking" is generally attributed to defects that can initiate fracture along a different path. The increased Mode I character of interlaminar lithium dendrites should reduce the driving force for dendrite kinking. Furthermore, the higher modulus of rGO (256.1 GPa)[49] compared to LLZTO (149.8 GPa)[50] will promote dendrite deflection along the interlayer, and stress redistribution at the crack tip should drive crack deflection along the interface until further delamination causes through-thickness kinking.[51] However, when this concept is extended to lithium dendrites, electric field effects can potentially enhance the tendency for kinking. The tradeoff between these elastic and electric field effects requires a detailed analysis of specific configurations and relevant material properties, including differences in elastic modulus, Poisson ratio, and the electrical and ionic conductivity between the interlayer and the solid electrolyte.[46,52]

The hypothesis that dendrite deflection at a PEO or rGO interface is similar to crack deflection is consistent with the results reported here, with weak interfacial bonding promoting dendrite deflection. It is important to note that the fundamental question of whether dendrite propagation through a solid electrolyte

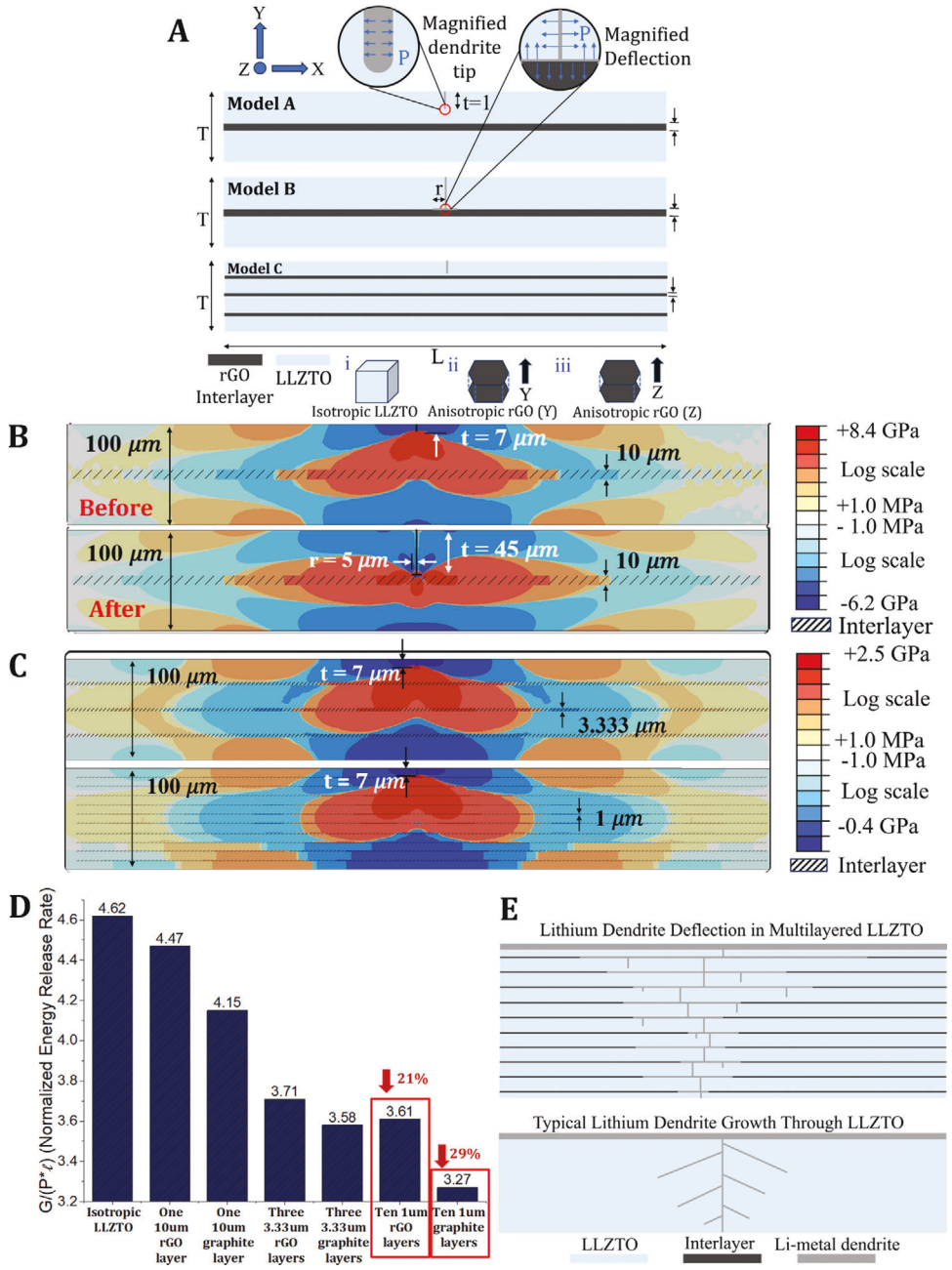

Figure 7. Lithium metal dendrite mitigation with multilayer structures. A) Three models each show a 2D cross-section of the LLZTO material with length $L = 10$ mm and thickness $T = 100$ μm and different interlayers. A centered seam-like crack (of length 1 and zero thickness) is built in Models A–C. The blue arrows show the applied pressure at the dendritic crack surface. Model A shows rGO-LLZTO with a 10um thin rGO interlayer. A deflection event (of length r) in Model B is conducted. The "Magnified Deflection" schematic shows the deflecting corner. Different normal plane directions, as shown in (i–iii), are implemented for anisotropic material properties of graphite and rGO. i) The light blue cube represents isotropic LLZTO. ii) layered dark gray hexagons with arrows in the Y direction represent anisotropic rGO whose normal plane is parallel to the interfacial plane. iii) layered dark gray hexagons with arrows in the *Z* direction represent anisotropic rGO whose normal plane is perpendicular to the interfacial plane. A right-hand coordinate system was employed to delineate directions within interlayers due to rGO's unidirectional anisotropy. B) The σ_{xx} stress fields (log scale) before (top) and after deflection (bottom) are shown: the symmetric tensile stress distribution at the dendrite tip changes to a compressive/tensile mixed stress state at the rGO interlayer interface. C) σ_{xx} stress fields (log scale), before the crack reaches the interlayer for two scenarios are shown: three 3.33 μm interlayers (top) and ten 1 μm thick interlayers (bottom). D) Normalized energy release rate ($G/(P \times \ell)$) at the crack tip for different interlayer materials. Substantial reductions in the energy release rate relative to isotropic LLZTO are observed with ten interlayers of rGO or graphite l (21% and 29%, respectively). E) Schematic showing dendrite deflection in multi-layered solid electrolyte structures (top) versus single-phase solid electrolyte (bottom). The multilayered structure greatly increases the "damage" tolerance of the solid electrolyte in terms of lithium dendrite penetration.

(without considering deflection) is "the same" as fracture is still an open research question.[7,8,12,30]

3. Multilayer Simulations

The observed deflection of lithium at an interlayer within a solid electrolyte successfully demonstrates that a layered structure can improve the resistance of the material to lithium dendrite penetration. For the multilayered structures investigated here, this is seen in the continued stable cycling that occurs after an initial short-circuit through one solid electrolyte layer and in the post-mortem images. In principle, this proof-of-concept architecture can be extended to a generalized electrolyte design with multiple interlayers to enable the creation of more "damage-tolerant" structures. These materials would be analogous to multilayered architectures that have been widely used to improve fracture resistance in a conventional context. A FEM was constructed to further explore the potential advantages of this type of structure, using J-Integral methods to evaluate the energy release rate of crack propagation and deflection.[17,53] This modeling also provides a detailed description of the stress distribution that arises when a dendrite reaches an internal interface. For this simulation, the cross-sectional surface of the LLZTO electrolyte is represented as a 2D sandwich-like beam (of length $L = 10\,000\ \mu m$ and thickness $T = 100\ \mu m$) with interlayers (of total N layers and $t = 10/\mathrm{N}\ \mu m$ thickness) and a dendritic crack (of length l) at the midpoint of the beam. The dendritic crack is modeled as a zero-thickness seam subjected to constant pressure (constant lithium plating flux into the dendrite) as the driving force. A uniform pressure is applied to element surfaces along the seam crack in general static steps. The value of the pressure (on the order of 100 MPa) corresponds to that needed for crack propagation (see Experimental Section for details) and is also consistent with direct experimental measurements.[13,54] This initial model employs a static fracture analysis to provide insight into the effect of tough interlayers on mitigating the driving forces for crack propagation. This simplified approach provides information about the impact of material heterogeneity on crack arrest that is potentially valuable for designing damage-tolerant solid electrolytes.

The three models in **Figure** 7A each show different 2D cross-sections of the LLZTO material with different interlayers. Model A shows rGO-LLZTO with a 10 µm thin rGO interlayer. A deflection event (of length r) of the crack upon reaching an interlayer is shown in Model B, using a similar seam-like crack. Model C is identical in construction to Model A, but with more interlayers. For a single interlayer, the stress fields in Figure 7B show that the elastic fields are much larger than the interlayer thickness. For multiple interlayers, complex stress distributions will occur, as seen in Figure 7C. The results of the simulation are summarized in Figure 7D and show that significant decreases in the energy release rate are expected with thin and stiff interlayer materials such as oriented graphite and rGO. With multiple engineered interlayers embedded into the electrolyte, the lithium dendrite potentially encounters deflection along at each interlayer (Figure 7E), drastically improving the critical current density of the laminated electrolyte and exhibiting substantially better overall resistance to dendrite penetration than our initial proof-of-concept experiments. Adding more interlayers, however, will most likely decrease the overall ionic conductivity of the solid electrolyte, leading to higher overall cell impedance. This points to a crucial balance between dendrite inhibition and the overall impedance.

4. Conclusion

This work demonstrates that chemo-mechanical fracture concepts can effectively describe dendrite deflection at bi-material interfaces in multilayered solid electrolytes. This initial study also indicates that, counterintuitively, a limited electron conductor embedded in the inner structure of a composite solid-state electrolyte can be advantageous in effectively suppressing lithium dendrite penetration at high current densities. A fracture-based model is developed to determine the criteria needed for lithium dendrite deflection at an inner interlayer within a solid electrolyte. An experimental design was then constructed to verify this mechanical model. A variety of interlayer materials were examined, including polymer electrolytes and fully metallic interlayers. An rGO interlayer material led to the most effective lithium dendrite deflection, allowing for partial short-circuiting of the cell but still cycling stably up to high critical current densities of ≈3.8 mA cm^{-2} (more than six times higher thanthe control cells without an rGO interlayer). Based on analysis of the experiments and finite element modeling, we propose that the superior performance of the rGO material is associated with the following:

- Deflection along the solid electrolyte/interlayer interface, due to a favorable strain energy release rate.
- High modulus and high through-thickness fracture resistance of the interlayer.
- Limited electron conduction of the interlayer, leading to localized lithiation of the interlayer material, along with redistribution of the electric field near the dendrite tip.

More broadly, these three mechanisms provide important guidelines for future design and optimization of multilayered solid electrolytes with superior properties.

5. Experimental Section

rGO-LLZTO Synthesis: LLZTO was purchased from Toshima (Japan). The LLZTO used in this study had a fracture resistance of 2.37–3.67 MPa $m^{0.5}$, with an average value of 2.87 MPa $m^{0.5}$, as measured through micro-indentation tests. Graphene oxide (GO) was synthesized and purified in-house using a modified Hummer's method following the procedure in Spitz et al.[55] Monolayer GO nanosheets were harvested into aqueous stock suspensions of 1–3 mg ml^{-1} to use as an ink for film casting. A 75 µL aliquot of 0.5 mg ml^{-1} GO suspension was pipetted onto one side of a LLZTO pellet. An LLZTO pellet was placed in an oven at 60 °C for 15 min to partially dry before placing another, clean LLZTO pellet on top. The GO film, lying between the two adhered LLZTO pellets, was left to dry overnight before heating in a tube furnace at 150 °C for 2 h for reduction.

PEO-LLZTO Synthesis: PEO powder (MW. 1 000 000, Sigma Aldrich) was dried in a vacuum furnace at 60 °C for 48 h to remove water and trace hydrates. To make the PEO solution, 20 mg of dried PEO powder was stirred thoroughly in 4 mL of acetonitrile solution for 12 h to form a PEO solution. To prepare the LLZTO for interlayer synthesis, polypropylene was painted along the edge of an LLZTO pellet to prevent solution leakage onto the sides to the LLZTO. The PEO solution was then drop-casted onto

the surface of the LLZTO. When most but not all of the acetonitrile had evaporated, a second LLZTO piece was placed on top of the drop-cast PEO layer to complete the PEO-LLZTO electrolyte. Finally, the PEO-LLZTO was placed on a hot plate at 50 °C in the glovebox for adhesion and drying.

PVdF-HFP-LLZTO Synthesis: PVdF-HFP powder was dried in a vacuum furnace at 60 °C for 48 h to remove water and trace hydrates. To make the PVdF-HFP solution, 20 mg of dried PVdF-HFP powder was powder stirred thoroughly in 4 mL of acetonitrile solution for 12 h to form a PVdF-HFP solution. As with the PEO-LLZTO, a polypropylene seal was created on the outer edge of a LLZTO pellet. The PVdF-HFP solution was then drop-casted onto the surface of the LLZTO. When most but not all the acetonitrile had evaporated, a second LLZTO piece was placed on top of the drop-cast PVdF-HFP layer to complete the PVdF-HFP-LLZTO electrolyte. Finally, the PVdF-HFP-LLZTO was placed on a hot plate at 50 °C in a glovebox for adhesion and drying.

In-LLZTO Synthesis: Indium metal (2.5 µm) was first deposited on LLZTO using a thermal evaporator integrated with a glovebox (Angstrom Engineering, Canada). To prevent indium deposition on the edges of the pellets, one side of the LLZTO pellets was covered with Kapton tape featuring a 10 mm diameter hole in the center. This precautionary measure helped to avoid potential short-circuiting between the working and countering electrodes. The deposition thickness was monitored using a quartz crystal microbalance, with a deposition rate of ≈3 Å s^{-1}. This rate was controlled by adjusting the heating power to the crucible. Two pieces of this indium-coated-LLZTO pellets were then stacked under pressure with the indium in contact and heat treated at 225 °C in a glovebox to thermally bond the indium together. The resulting In-LLZTO was then cooled to room temperature.

c-LLZTO Synthesis: c-LLZTO was created in a similar fashion to rGO-LLZTO and PEO-LLZTO. The edges of the LLZTO were coated with polypropylene to prevent liquid from leaking onto the sides of the ceramic discs. A drop of 0.6 M Lithium bis(trifluoromethane) sulfonimide (LiTFSI) and 0.4 M $LiNO_3$ in Dioxolane (DOL)/ Dimethoxyethane (DME) (1:1 volume ratio) liquid electrolyte was placed on the bottom LLZTO piece with a volumetric pipette. The second LLZTO disc was placed directly on top of this before drying.

rGO Lithiation Reference Cell Synthesis: A piece of copper foil was sonicated for 45 min in ethanol and dried thoroughly. The copper foil was punched to the same size as the LLZTO to act as the current collector. As with rGO-LLZTO, an LLZTO disc was heat treated at 500 °C for 4 h and polished with a silica carbide polishing paper to remove contaminants from the surface. A 75 µL aliquot of 0.5 mg ml^{-1} GO suspension was pipetted onto one side of a LLZTO pellet. A copper current collector was placed on top of the drop-cast rGO layer to complete the rGO lithiation reference cell. The GO film was left to dry overnight before heating in a tube furnace at 150 °C for 2 h for reduction.

Coin Cell Synthesis: The coin cell synthesis procedure was identical regardless of the different laminated electrolytes used. All cells were assembled in CR2032-type coin cells in an Argon-filled glovebox (O_2 and H_2O < 0.1 ppm). The lithium metal foil surface was first brushed until shiny to remove contaminants from the surface. Lithium metal electrodes with a diameter of 6.5 mm were punched from the lithium metal foil and placed on both sides of the solid laminated electrolyte to create a Li||Li symmetric coin cell. In order to maintain ionic contact between the lithium electrode and LLZTO surface during the duration of electrochemical cycling, a small drop (<10 µL) of 0.6 M LiTFSI and 0.4 M $LiNO_3$ in DOL/DME (1:1 volume ratio) liquid electrolyte was dropped onto the surface of the Li metal electrode on both sides in order for the cell to cycle at reasonable overpotentials. Likewise, the edges of the LLZTO were coated with polypropylene to prevent liquid from leaking onto the sides of the ceramic discs. This approach was used in recent research to improve the surface wetting of the Li-anode/LLZTO surface.[56,57] The crux of this project was to investigate the mechanical deflection of lithium dendrites, and thus additional surface interface modifications to improve overall performance were not used.

Three-Electrode Coin Cell Synthesis: Three-electrode cells were simply a slightly modified version of rGO-LLZTO, with the only additional piece being the copper tab. The copper tab was first cut from a piece of thin copper foil. The tab was approximately 4 cm long and 0.5 cm wide. Kapton tape was used to fully wrap the middle section of the copper tab, exposing ≈1 cm of copper on each end. The electrolyte synthesis was nearly identical to rGO-LLZTO. Before the second LLZTO piece was placed onto the bottom LLZTO disc and rGO interlayer, one end of the copper tab was carefully rested on the rGO interlayer. The second LLZTO piece was then placed on to cover the copper tab and the rGO. When sealing the coin cell, the middle section (with Kapton tape) of the copper tab was sealed in contact with the sides of the coin cell to avoid electrical contact.

Electrochemical Measurements: All electrochemical measurements were made after resting each coin cell for 2 h. A battery cycler (Biologic, SP300) was employed to measure the voltage curves of the cells under plating-only sequences. The sequences were designed to begin plating at a current density of 0.1 mA cm^{-2} with a 1 mAh cm^{-2} capacity limit and with a ramp-up step of 0.05 mA cm^{-2}. EIS measurements were conducted on a Biologic SP300 over a frequency range from 10^{-3} to 10^{6} Hz using AC perturbation of 10 mV. Three-electrode OCV measurements were made by simply connecting a third electrode alligator clip to the extended copper tab. All electrochemical measurements were made at room temperature.

Post-Mortem Imaging: Each laminated electrolyte was marked into four quadrants by a permanent marker to better observe the discrepancy in the location of the dendritic penetration sites. The lithium plated on the rGO interlayer was imaged. P1200 grit silica carbide polishing paper was used to carefully polish off the excess lithium metal and rGO and expose the LLZTO discs underneath. The LLZTO discs were imaged. A thin razor blade was used to slice the LLZTO among a dendritic penetration line and examined with a Scanning Electron Microscopy (SEM, ThermoScientific Quattro S ESEM) using an acceleration voltage of 10–20 kV.

Finite Element Modeling Details: LLZTO was modeled as an isotropic material with two elastic constants. Previous works have calculated the shear modulus and Poisson's ratio.[49,50] In this FEM simulation, the Young's modulus was calculated through the shear modulus and Poisson's ratio. As anisotropic materials, rGO and graphite were both described as tetragonal symmetric with 6 elastic constants each. Previous work[58] reports all elastic constants for rGO and graphite at room temperature. In this study, elastic constants were transformed to engineering constants such as Young's modulus, shear modulus, and Poisson's ratio, which are more widely used in simulation material property settings. The specific elastic constants used can be found in the Supporting Information.

A right-hand coordinate system was employed to delineate directions within interlayers due to rGO's unidirectional anisotropy. The X–Z plane in Figure 7C represents the interfacial plane of the electrolyte and rGO interlayers. The Y direction represents the thickness of the multilayer electrolyte. Three material property scenarios were examined: 1) isotropic properties using LLZTO's Young's modulus and shear modulus as a reference case; 2) anisotropic properties using rGO's elastic constants; 3) anisotropic properties using graphite's elastic constants. The main geometry included a limited number of Constant Phase Element 3 (CPE3, three-node plane strain) elements and over 10,000 CPE4 (four-node plane strain) elements, while an additional 5000 finer CPE4 elements were specifically positioned in the crack tip field to enhance J-integral calculations using the contour integral method.

The value of the pressure (100 MPa) corresponds to that needed for crack propagation. (Using the basic stress intensity factor equation and an approximate fracture toughness that is close to the reported value for LLZTO,[59] the criteria for fracture is:

$$K_I = \frac{\pi}{2}\, p\, \sqrt{l} = K_{1C} \rightarrow p = \frac{2K_{1c}}{\pi\sqrt{l}} \approx 100\ MPa \tag{6}$$

This corresponds to the l value of 45 µm in Figure 7A. For ease of comparison between the cases with one, three, and ten interlayers, the applied pressure in all cases was set at 100 MPa.

The energy release rate in these calculations is given by:

$$G = \frac{K_I^2}{E'_{SE}} = C\frac{p^2 l}{E'_{SE}} \quad (7)$$

where the constant C is a geometric coefficient that depends on the number of layers in the electrolyte. The results plotted in Figure 7, then show the dimensionless energy release rate:

$$\frac{G}{pl} = C\frac{p}{E'_{SE}} \quad (8)$$

The energy release rate G at the crack tip field was calculated as the steps progressed with the J integral method. Although the normalized energy release rate varied with applied pressure (since the applied pressure was fixed at 100 MPa for all cases), this normalized energy release rate was now a function of only geometry (i.e., the effect of different number layers). In Figure 7D's simulation, the effect of the applied load was canceled out with the normalized energy release rate expression, to focus only on the shape coefficients with a different number of interlayers. The J-integral remained path-independent because the contour integral was restricted entirely within a single, homogeneous material layer—specifically, the first electrolyte layer where lithium dendrite initiation occurs. Within this layer, no material inhomogeneity existed, and thus the assumptions underlying the J-integral's path-independence (homogeneity and monotonic stress–strain relations) were valid.

The interface in the simulation was treated as tightly bonded using a "TIE" interaction condition. Regarding the validation of this interface treatment, while the simulation assumed perfect bonding, the elastic mismatch between the solid electrolyte and rGO was still captured in the stress distribution, as demonstrated in Figures 7B,C. The stress response illustrated how the inhomogeneity between these two materials manifested under load, even with the assumption of a tightly bonded interface. From a simulation standpoint, one method to assess whether tight bonding was a valid description was to compare the interfacial adhesion energy with the energy release rate due to elastic mismatch. If the energy release rate exceeded the interfacial adhesion energy, debonding should occur at the interface. In such cases, a different interfacial treatment—such as cohesive zone modeling—would be necessary to capture the opening of new surfaces and the loss of bonding. In this study, the experimental observations described in the manuscript indicated weak adhesion between the solid electrolyte and the rGO. This experimental evidence was aligned with the simulation and supported the assumption that the interface behaved as weakly bonded under the conditions that were investigated, further validating the modeling approach.[17,53]

Supporting Information

Supporting Information is available from the Wiley Online Library or from the author.

Acknowledgements

This work was supported by NSF Grant DMR – 2124775.

Conflict of Interest

Brown University has filed for patents on subject matter related to this manuscript in which Z.Y., C.S. and B.W.S. are listed inventors.

Author Contributions

Z.Y. and B.W.S. conceptualized the study. Z.Y. and C.S. designed and executed the experiments and analyzed the data with input from B.W.S. C.G. developed the Finite-element model and analysis with input from A.M. and B.W.S. A.S. and R.H. synthesized rGO material used in this work. C.L.P. assisted with post-mortem characterization, including Raman Spectroscopy. X.C.X. assisted with PVD coating of Indium layers onto LLZTO. B.W.S. developed the concepts for the mechanics of deflection in a multi-layered electrolyte. Z.Y. wrote the first draft of the manuscript.

Data Availability Statement

The data that support the findings of this study are available from the corresponding author upon reasonable request.

Keywords

crack deflection mechanics, electro-chemo-mechanics, fracture mechanics, lithium dendrite suppression, mixed conductors, multi-layered solid electrolytes

Received: July 20, 2024
Revised: October 18, 2024
Published online: November 24, 2024

[1] T. Krauskopf, F. H. Richter, W. G. Zeier, J. Janek, *Chem. Rev.* **2020**, *120*, 7745.
[2] A. Manthiram, X. W. Yu, S. F. Wang, *Nat. Rev. Mater.* **2017**, *2*, 16103.
[3] Q. Zhao, S. Stalin, C.-Z. Zhao, L. A. Archer, *Nat. Rev. Mater.* **2020**, *5*, 229.
[4] T. Famprikis, P. Canepa, J. A. Dawson, M. S. Islam, C. Masquelier, *Nat. Mater.* **2019**, *18*, 1278.
[5] R. Murugan, V. Thangadurai, W. Weppner, *Angew. Chem., Int. Ed.* **2007**, *46*, 7778.
[6] P. Albertus, V. Anandan, C. Ban, N. Balsara, I. Belharouak, J. Buettner-Garrett, Z. Chen, C. Daniel, M. Doeff, N. J. Dudney, B. Dunn, S. J. Harris, S. Herle, E. Herbert, S. Kalnaus, J. A. Libera, D. Lu, S. Martin, B. D. McCloskey, M. T. McDowell, Y. S. Meng, J. Nanda, J. Sakamoto, E. C. Self, S. Tepavcevic, E. Wachsman, C. Wang, A. S. Westover, J. Xiao, T. Yersak, *ACS Energy Lett.* **2021**, *6*, 1399.
[7] L. Porz, T. Swamy, B. W. Sheldon, D. Rettenwander, T. Frömling, H. L. Thaman, S. Berendts, R. Uecker, W. C. Carter, Y.-M. Chiang, *Adv. Energy Mater.* **2017**, *7*, 2101807.
[8] C. H. Yuan, W. Q. Lu, J. Xu, *Adv. Energy Mater.* **2021**, *11*, 2101807.
[9] M. Klinsmann, F. E. Hildebrand, M. Ganser, R. M. McMeeking, *J. Power Sources* **2019**, *442*, 227226.
[10] D. Cao, X. Sun, Q. Li, A. Natan, P. Xiang, H. Zhu, *Matter* **2020**, *3*, 57.
[11] W. Wang, J. Wang, C. Lin, H. Ruan, *Adv. Funct. Mater.* **2023**.
[12] C. Yuan, X. Gao, Y. Jia, W. Zhang, Q. Wu, J. Xu, *Nano Energy* **2021**, *86*, 106057.
[13] C. D. Fincher, C. E. Athanasiou, C. Gilgenbach, M. Wang, B. W. Sheldon, W. C. Carter, Y.-M. Chiang, *Joule* **2022**, *6*, 2794.
[14] S. Kalnaus, N. J. Dudney, A. S. Westover, E. Herbert, S. Hackney, *Science* **2023**, *381*, 1300.
[15] C. E. Athanasiou, M. Y. Jin, C. Ramirez, N. P. Padture, B. W. Sheldon, *Matter* **2020**, *3*, 212.
[16] Y. Qi, C. M. Ban, S. J. Harris, *Joule* **2020**, *4*, 2599.
[17] M. Y. He, J. W. Hutchinson, *Int. J. Solids Struct.* **1989**, *25*, 1053.
[18] L. Cheng, M. Sun, F. Ye, Y. Bai, M. Li, S. Fan, L. Zhang, *Int. J. Lightweight Mater. Manuf.* **2018**, *1*, 126.
[19] K. Zhang, B. Gao, M. Gong, Z. Tong, J. Fan, *Ceram. Int.* **2022**, *48*, 21370.
[20] C. H. Yuan, B. W. Sheldon, J. Xu, *Adv. Energy Mater.* **2022**, *12*, 2201804.
[21] L. Ye, X. Li, *Nature* **2021**, *593*, 218.

[22] B. Hu, S. Zhang, Z. Ning, D. Spencer-Jolly, D. L. R. Melvin, X. Gao, J. Perera, S. D. Pu, G. J. Rees, L. Wang, L. Yang, H. Gao, S. Marathe, G. Burca, T. J. Marrow, P. G. Bruce, *Joule* **2024**, *8*, 2623.
[23] J. S. Kim, G. Yoon, S. Kim, S. Sugata, N. Yashiro, S. Suzuki, M. J. Lee, R. Kim, M. Badding, Z. Song, J. Chang, D. Im, *Nat. Commun.* **2023**, *14*, 3201.
[24] K. Lee, S. Han, J. Lee, S. Lee, J. Kim, Y. Ko, S. Kim, K. Yoon, J.-H. Song, J. H. Noh, K. Kang, *ACS Energy Lett.* **2022**, *7*, 381.
[25] F. J. Zhu, W. Deng, B. Zhang, H. Wang, L. Xu, H. Liu, Z. Luo, G. Zou, H. Hou, X. Ji, *Nano Energy* **2023**, *111*.
[26] Z. Wang, J. Tan, J. Cui, K. Xie, Y. Bai, Z. Jia, X. Gao, Y. Wu, W. Tang, *J. Mater. Chem. A* **2024**, *12*, 4231.
[27] X. Zhu, K. Wang, Y. Xu, G. Zhang, S. Li, C. Li, X. Zhang, X. Sun, X. Ge, Y. Ma, *Energy Storage Mater.* **2021**, *36*, 291.
[28] H.-S. Shin, W.-G. Ryu, M.-S. Park, K.-N. Jung, H. Kim, J.-W. Lee, *ChemSusChem* **2018**, *11*, 3184.
[29] J. W. Hutchinson, Z. Suo, in *Adv. Appl. Mech.*, **1991**, J. W. Hutchinson, T.Y. Wu, Eds. Elsevier, p. 63.
[30] M. K. Rahman, M. M. Hossain, S. S. Rahman, *Int. J. Fract.* **2000**, *103*, 243.
[31] B. K. Ahn, W. A. Curtin, T. A. Parthasarathy, R. E. Dutton, *Compos. Sci. Technol.* **1998**, *58*, 1775.
[32] A. Gupta, J. Sakamoto, *Electrochemical Society Interface* **2019**, *28*, 63.
[33] H. S. Xu, S. Huang, J. Qian, S. Liu, L. Li, X. Zhao, W. Zhang, *Colloids Surf., A* **2022**, 653.
[34] Z. Li, H. M. Huang, J. K. Zhu, J. F. Wu, H. Yang, L. Wei, X. Guo, *ACS Appl. Mater. Interfaces* **2019**, *11*, 784.
[35] W. He, H. Ding, X. Chen, W. Yang, *J. Membr. Sci.* **2023**, *665*, 121095.
[36] C. Shi, T. Hamann, S. Takeuchi, G. V. Alexander, A. M. Nolan, M. Limpert, Z. Fu, J. O'Neill, G. Godbey, J. A. Dura, E. D. Wachsman, *ACS Appl. Mater. Interfaces* **2022**, *15*, 751.
[37] F. Chen, M.-X. Jing, H. Yang, W.-Y. Yuan, M.-Q. Liu, Y.-S. Ji, S. Hussain, X.-Q. Shen, *Ionics* **2021**, *27*, 1101.
[38] S. B. Ye, B. Chen, J. C. Feng, *Sci. Rep.* **2015**, *5*, 13102.
[39] E. Maccaferri, J. Ortolani, L. Mazzocchetti, T. Benelli, T. M. Brugo, A. Zucchelli, L. Giorgini, *ACS Omega* **2022**, *7*, 23189.
[40] R. Kumar, M. K. Rangswamy, D. Lahiri, I. Lahiri, *Surf. Coat. Technol.* **2017**, *309*, 931.
[41] D. W. Kang, S. J. Lee, G. H. Ryu, M. Lee, J-H Kim, *Appl. Surf. Sci.* **2023**, *624*, 157121.
[42] R. Straessle, Y. Pétremand, D. Briand, M. Dadras, N. F. de Rooij, *J. Micromech. Microeng.* **2013**, *23*, 075007.
[43] R. Straessle, Y. Petremand, D. Briand, N. F. De Rooij, *Proc. Eng.* **2011**, *25*, 1493.
[44] J. H. Cho, K. Kim, S. Chakravarthy, X. Xiao, J. L. M. Rupp, B. W. Sheldon, *Adv. Energy Mater.* **2022**, *12*, 2200369.
[45] E. J. Cheng, A. Sharafi, J. Sakamoto, *Electrochim. Acta* **2017**, *223*, 85.
[46] J. P. Parmigiani, M. D. Thouless, *J. Mech. Phys. Solids* **2006**, *54*, 266.
[47] E. Santos, W. Schmickler, *Angew. Chem., Int. Ed.* **2021**, *60*, 5876.
[48] A. Aryanfar, D. Brooks, B. V. Merinov, W. A. Goddard, A. J. Colussi, M. R. Hoffmann, *J. Phys. Chem. Lett.* **2014**, *5*, 1721.
[49] J. E. Ni, E. D. Case, J. S. Sakamoto, E. Rangasamy, J. B. Wolfenstine, *J. Mater. Sci.* **2012**, *47*, 7978.
[50] S. Yu, R. D. Schmidt, R. Garcia-Mendez, E. Herbert, N. J. Dudney, J. B. Wolfenstine, J. Sakamoto, D. J. Siegel, *Chem. Mater.* **2016**, *28*, 197.
[51] P. M. Pohl, F. Kümmel, C. Schunk, I. Serrano-Munoz, H. Markötter, M. Göken, H. W. Höppel, *Materials* **2021**, *14*, 2564.
[52] B. M. Sundaram, H. V. Tippur, *J. Mech. Phys. Solids* **2016**, *96*, 312.
[53] A. Abdul-Aziz, R. T. Bhatt, J. E. Grady, *Mech. Adv. Mater. Struct.* **2015**, *22*, 1039.
[54] C. E. Athanasiou, C. D. Fincher, C. Gilgenbach, H. Gao, W. C. Carter, Y-M Chiang, B. W. Sheldon, *Matter* **2024**, *7*, P95.
[55] R. Spitz Steinberg, M. Cruz, N. G. A. Mahfouz, Y. Qiu, R. H. Hurt, *ACS Nano* **2017**, *11*, 5670.
[56] S. Mu, W. Huang, W. Sun, N. Zhao, M. Jia, Z. Bi, X. Guo, *J. Energy Chem.* **2021**, *60*, 162.
[57] M. Liu, W. Xie, B. Li, Y. Wang, G. Li, S. Zhang, Y. Wen, J. Qiu, J. Chen, P. Zhao, *ACS Appl. Mater. Interfaces* **2022**, *14*, 43116.
[58] R. J. Jiménez Riobóo, E. Climent-Pascual, X. Díez-Betriu, F. Jiménez-Villacorta, C. Prieto, A. de Andrés, *J. Mater. Chem. C* **2015**, *3*, 4868.
[59] R. J.-Y. Park, C. M. Eschler, C. D. Fincher, A. F. Badel, P. Guan, M. Pharr, B. W. Sheldon, W. C. Carter, V. Viswanathan, Y.-M. Chiang, *Nat. Energy* **2021**, *6*, 314.